On the role played by turbulence closures for the vortex-vortex interactions of an aircraft

E Guilmineau, M Visonneau

On the role played by turbulence closures for the vortex-vortex interactions of an aircraft

E. GUILMINEAU[a], M. VISONNEAU[b]

a. LHEEA-CNRS UMR 6598, Centrale Nantes, emmanuel.guilmineau@ec-nantes.fr
b. LHEEA-CNRS UMR 6598, Centrale Nantes, michel.visonneau@ec-nantes.fr

Résumé :

Dans cette étude, des simulations numériques d'écoulement autour d'un avion avec plus ieurs angles d'attaque et avec un angle de dérapage modéré sont effectuées avec le code ISIS-CFD qui utilise les équations de Navier-Stokes moyennées instationnaire pour un fluide incompressible. La modélisation de la turbulence est réalisée à l'aide du modèle isotrope linéaire k-ω SST et du modèle hybride RANS/LEs DDES-SST. Pour chaque fermeture de la turbulence, la fonctionnalité du raffinement de maillage adaptatif et anisotrope est utilisée. Les coefficients aérodynamiques ainsi que des données de champ d'écoulement sont comparées aux mesures expérimentales. La principale conclusion est que les simulations numériques avec le modèle DDES-SST sont en meilleur accord avec les mesures expérimentales que les simulations avec le modèle k-ω SST.

Abstract :

In the present work, numerical simulations of the flow around an aircraft at several angles of attack and with a moderate drift angle are performed with the ISIS-CFD flow solver which is an incompressible unsteady Reynolds-averaged Navier-Stokes method. The turbulence modelling is performed using the linear isotropic k-ω SST model and the hybrid RANS/LES DDES-SST model. For every turbulence closure, the anisotropic adaptive grid refinement functionality is used. Aerodynamic coefficients as well as flow field data are compared with experimental measurements. The main conclusion is that the numerical simulations with the DDES-SST model are in better agreement with the experimental data than the simulations with the k-ω SST.

Key works : Turbulence models, Aircraft, Numerical simulation, ISIS-CFD, NATO/AVT-316

1 Introduction

High-agile high performance aircraft configurations have to cover a wide scope of performance and maneuverability requirements from an supersonic cruise to a high maneuverability at subsonic conditions [6]. Hybrid-delta wings present many assets for the aerodynamic design of high agility military aircraft. The flow over such wings is dominated by multiple vortices. When the angle of attack increases, the vortices start interacting with each other enabling a more stable vortex system. For high angles of

attack, the vortex breaks down resulting in an increasing pitching moment and a decrease in the gradient of lift coefficient [1]. An extensive synthesis of CFD simulations for the F16-XL configurations, which has a triple-delta-wing configuration, has been conducted [9] using hybrid RANS/LES methods which predicted correctly the vortical characteristics.

A low-aspect ratio multiple-swept wing fuselage is studied in the NATO STO AVT-316 task group on "Vortex Interaction Effects Relevant to Military Air Vehicle Performance". This collaborative research has been initiated to assess Computational Fluid Dynamics (CFD) methods to predict vortex-interaction effects and extend the understating of vortex-interaction flow physics for these problems through numerical and physical experimentation.

In this paper, we conduct a numerical simulation of the flow past the wing-fuselage combination at Mach number 0.15 for several angles of attack with a side slip angle, by means of RANS and hybrid RANS/LES simulations. A comparison will be carried out between the numerical simulations and experimental data.

2 Test case

Figure 1 illustrates the test configurations [7, 11]. The first one is a triple delta wing configuration, the so-called NA1-W1, see Figure 1(a), with three different consecutive wing sections featuring a varying leading-edge sweep. The inboard and outboard wing sections exhibit a medium leading-edge sweep of $\varphi_1 = \varphi_3 = 52.5°$ and the mid-board wing section is highly swept at $\varphi_2 = 75.0°$. The second one is a double delta configuration, the so-called NA1-W2, see Figure 1(b), with two different consecutive wing sections of varying leading-edge sweeps characterized by a high leading-edge sweep of $\varphi_2 = 75.0°$ in the inboard wing section and a medium leading-edge sweep of $\varphi_3 = 52.5°$ in the outboard wing section. Both configurations have the same total length of $l_{tot} = 1.160$ m and the same root chord of $c_r = 0.802$ m.

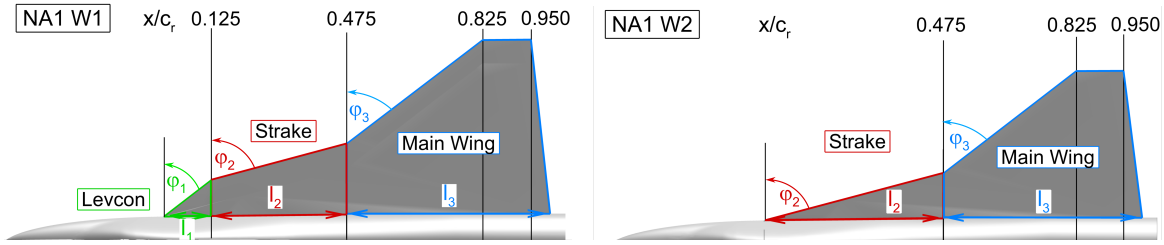

(a) NA1-W1 model. (b) Model NA1-W2.

FIGURE 1 – Wing planforms.

Experiments are conducted in the wind tunnel of Technical University of Munich (TUM) for a speed of $V_\infty = 51.97$ m/s, which leads to a Reynolds number, based on c_r, of 2.36×10^6 and a Mach number of 0.15. Two side slip angles, β, are investigated $0°$ and $5°$.

3 Flow solver

The in-house solver ISIS-CFD developed by the authors, also available as a part of the FINE™/Marine computing suite worldwide distributed by Cadence Design Systems, is an incompressible multiphase unsteady Reynolds-averaged Navier-Stokes (URANS) solver mainly devoted to marine hydrodynamics. It is based on a fully-unstructured (face-based) finite volume discretization with specific functionalities

needed for multiphase flows and industrial applications [8, 12]. The method features several sophisticated turbulence models : apart from the classical two-equation k-ϵ and k-ω models, the anisotropic two-equation Explicit Algebraic Reynolds Stress Model (EARSM), as well as Reynolds Stress Transport Models, are available [2, 3, 4]. All models are available with wall-function or low-Reynolds near wall formulations. Hybrid RANS/LES turbulence models based on Detached Eddy Simulation (DES-SST, DDES-SST, IDDES-SST) are also implemented and have been thoroughly validated on automotive flows characterized by large separations [5] and ships at steady drift [13]. Moreover, the solver accepts sliding and overset grids and features an anisotropic adaptive grid refinement functionality [10, 14] applied to unstructured hexahedral meshes.

4 Numerical simulation set-up

The two exprimentally studied slip angles are used in this study. The turbulence models used are k-ω SST 2003 for the RANS model and DDES-SST for the hybrid RANS/LES modelisation. The time step used with the k-ω SST model is $\Delta t = 1.5 \times 10^{-4}$s and $\Delta t = 5 \times 10^{-5}$s with the DDES-SST model. The averaging time, tU_∞/c_r, varies between 30 and 60 depending on the case. Generally, the CPU time of a DDES similation is 5 times more expensive than a simulation with the k-ω SST model.

The meshes are generated using Hexpress™, an automatic unstructured mesh generator. This software generates meshes containing only hexahedrals. For the aircraft and the sting, no-slip boundary conditions are imposed and the wall normal resolution has y^+ below 1.

During the simulation, the average-based mesh adaptation procedure, included in ISIS-CFD, is also used, choosing as refinement criterion the flux component Hessian. The grid is adapted every 10 time steps. As the flow depends on the turbulence model, the number of cells varies depending on the turbulence model and the angle of attack α. Thus the number of cells varies between 5M and 130M. Figures 2 and 3 show an example of the mesh at cross-section $x/c_r = 0.475$ for $\alpha = 24°$ and $\beta = 5°$ for the geometries NA1-W1 and NA-W2, respectively.

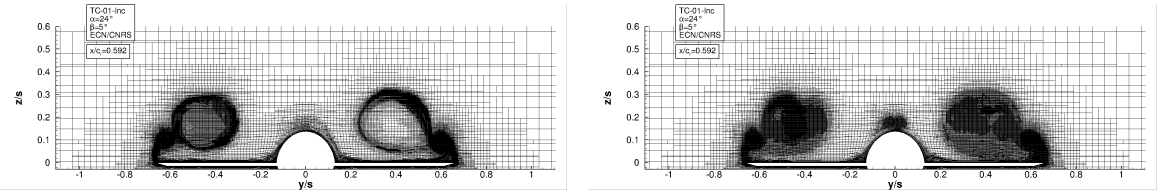

(a) k-ω SST. (b) DDES-SST.

FIGURE 2 – NA1-W1 : $\alpha = 24°$, $\beta = 5°$ - View of the flow adapted grids at the cross-section $x/c_r = 0.592$.

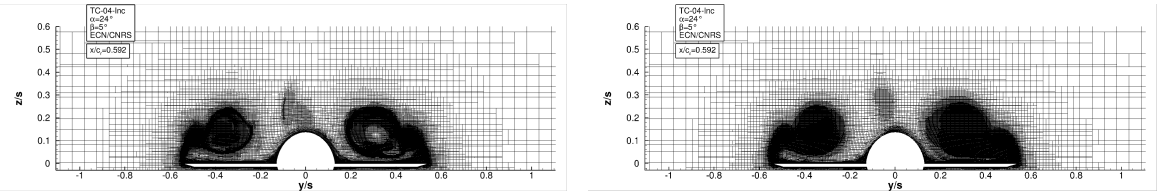

(a) k-ω SST. (b) DDES-SST.

FIGURE 3 – NA1-W2 : $\alpha = 24°$, $\beta = 5°$ - View of the flow adapted grids at the cross-section $x/c_r = 0.592$.

5 Results

5.1 Symmetric free-stream condition : β = 0°

5.1.1 Forces and moments

Figure 4 shows the evolution of the drag coefficient, C_D, the lift coefficient, C_L, and the pitching moment coefficient, C_{my}, versus the angle of attack, α, for the NA1-W1 and NA1-W2 configurations at $\beta = 0°$. For the configuration NA1-W1, see Figure 4(a), the numerical results are in very good agreement with the experimental data, except for α = 32°. It is a bit disappointing to see that the hybrid RANS/LES DDES-SST closure does not bring any significant improvement at this high angle of attack. The shape variation of the pitching moment curve around the angle of attack 12°, due to the onset of vortex breakdown at the trailing edge, is well predicted with the k-ω SST model, which is very satisfactory. For the configuration NA1-W2, see Figure 4(b), the vortex breakdown, observed at α = 23° in the experiments, leads to a local reduction of the lift coefficient. This local reduction of the lift is also predicted by the numerical simulations but at a smaller angle α = 20° with the k-ω SST. The same behaviour is observed on the pitch moment C_{my} whose abrupt increase occurring in the experiments at α = 23°, is predicted too early at α = 20°. For higher angles of attack, the lift predicted by $k-\omega$ SST continues to grow without being able to represent the plateau observed in the experiments from α = 28°. Although the hybrid RANS-LES closure does not provide significantly better simulation in this range of moderate angles of attack, i.e. for α comprised between 20° and 24°, it is reassuring to see that its prediction of drag, lift and pitch moment at a high angle of attack α = 32°, is now in perfect agreement with TUM measurements.

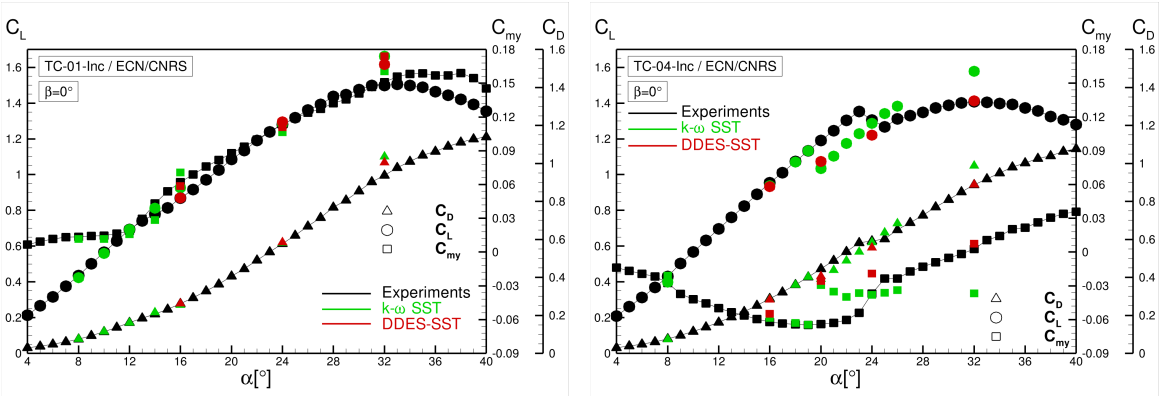

(a) NA1-W1 geometry.

(b) NA1-W2 geometry.

FIGURE 4 – β = 0° - Longitudinal aerodynamics coefficients versus the angle of attack α for both geometries.

5.1.2 Angle of attack α = 16°

Figure 5 presents the vortical structures obtained with both turbulence models for the angle of attack α = 16° and both wing configurations. These figures show the isosurface of the dimensionless second invariant, Q^* = 50, the blue translucent surface, and the zero-isosurface of the Cartesian axial component of the velocity, the red surface, which indicates a reverse flow. For NA1-W1, the flow is characterized by two primary leading-edge vortices. The first vortex develops at the most inboard wing section and

is called inboard vortex (IBV). The second vortex develops at the kink from the highly swept to the medium swept wing section at $x/c_r = 0.475$ and is called mid-board vortex (MBV). All these structures are predicted by every turbulence model. However, the size of these structures is thinner with the DDES-SST model, indicating more intense vortices. For the second wing configuration NA1-W2, k-ω SST predicts a similar unique IBV vortex while DDES-SST simulation provides a collection of peripheral vortices spiraling around a thinner vortex. The interaction with the second vortex MBV, originating from the medium swept wing, leads to a local zone of reverse flow as indicated by the red region which occurs more upstream than in the NA1-W1 configuration for both turbulence models. However, for DDES-SST, the detached layer simulated by k-ω SST is replaced by a collection of individual thinner longitudinal vortices originating from the leading edge of the medium swept wing, see Fig. 5(d).

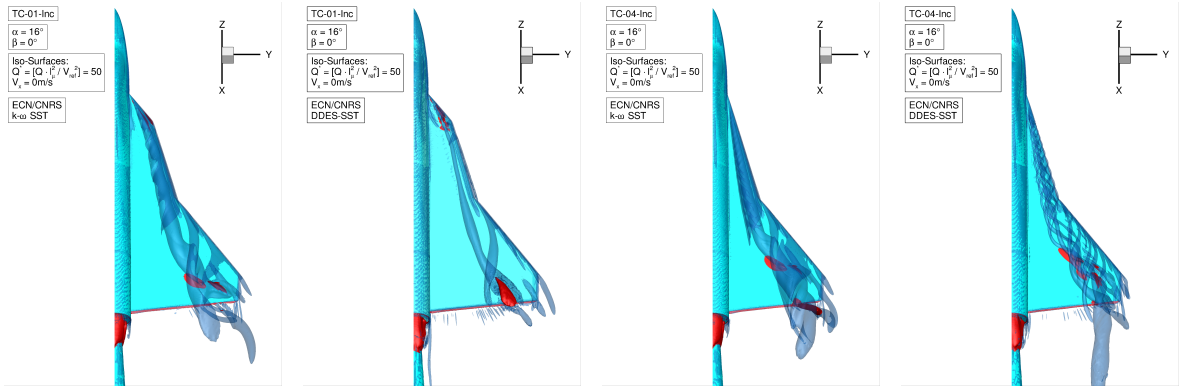

(a) NA1-W1 - k-ω SST. (b) NA1-W1 - DDES-SST. (c) NA1-W2 - k-ω SST. (d) NA1-W2 - DDES-SST.

FIGURE 5 – $\beta = 0°$ $\alpha = 16°$ - Vortical structures of the NA1-W1 and NA1-W2 configurations.

Figure 6 shows the dimensionless axial velocity component at the cross-section x/c_r=0.475 for the NA1-W1 geometry. Results obtained with k-ω SST and DDES-SST turbulence closures are compared with TUM experiments. First of all, the IBV vortex in the experiments shows a beginnig of wake-type. This characteristic is not well captured by k-ω SST model while DDES-SST simulation provides a very accurate solution which captures this characteristic evolution in the core of the main vortex. The MBV vortex is also more intense with DDES-SST and in better agreement with TUM experiments.

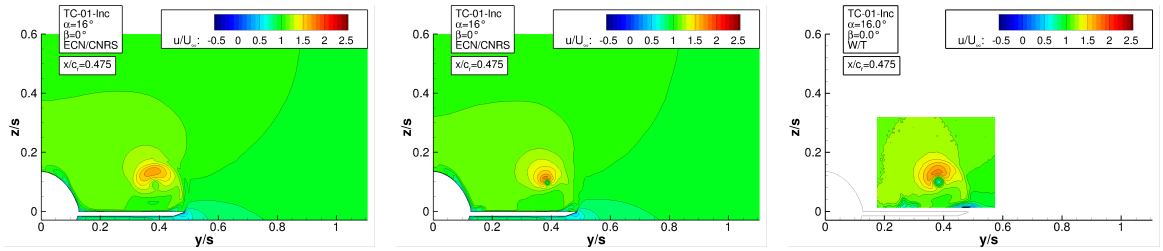

(a) k-ω SST. (b) DDES-SST. (c) TUM Experiments.

FIGURE 6 – $\beta = 0°$, $\alpha = 16°$, NA1-W1 - Axial component of the velocity at $x/c_r = 0.475$.

Figure 7 shows the dimensionless axial velocity component at the same cross-section the NA1-W2 geometry. Results obtained with k-ω SST and DDES are again compared with TUM experiments. The IBV vortex in the experiments has a jet-type. Both turbulence models predict this behavior. However with the DDES-SST model, the velocity in the core of the vortex is higher than the velocity obtained in the experiments.

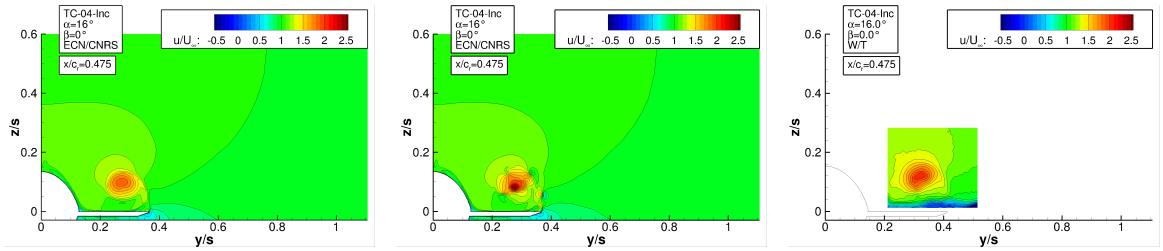

(a) k-ω SST. (b) DDES-SST. (c) TUM Experiments.

FIGURE 7 – β = 0° , α = 16° , NA1-W2 - Axial component of the velocity at x/c_r = 0.475.

5.1.3 Angle of attack α = 24°

Figure 8 presents the vortical structures obtained by the two turbulence models for the angle of attack α = 24° and both wing configurations. For NA1-W1, both IBV and MBV vortices are present with a reverse flow in the core of IBV starting earlier than for the previous angle of attack. Both turbulence closures predict the existence of a third vortex parallel to the fuselage during the first part of its path and then deviated towards the outer part of the wing, leading to a potentially more complex vortex interaction than for the lower angle of attack. For NA1-W2, the two main vortices IBV and MBV are present with a reverse flow starting later. Moreover, the third vortex emanating close to the fuselage is also found for this wing but its path remains parallel to the fuselage.

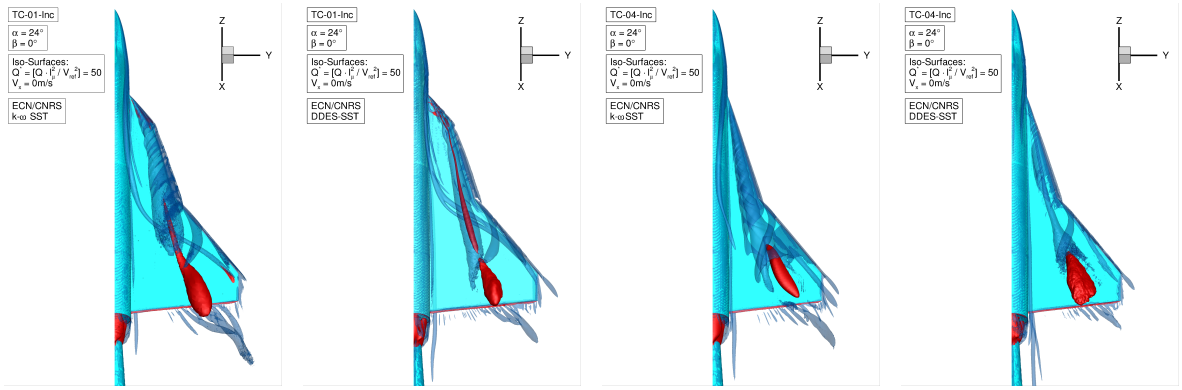

(a) NA1-W1 - k-ω SST. (b) NA1-W1 - DDES-SST. (c) NA1-W2 - k-ω SST. (d) NA1-W2 - DDES-SST.

FIGURE 8 – β = 0° α = 24° - Vortical structures of the NA1-W1 and NA1-W2 configurations.

Figure 9 shows the axial velocity component at the cross-section x/c_r=0.475 for the NA1-W1 geometry. As observed previously for α = 16°, the IBV vortex has a marked wake-type illustrated by the large region of very low axial velocity in its core at this cross-section. k-ω SST predicts qualitatively this trend but still over-estimates the axial velocity in the core of IBV. On the contrary, DDES-SST captures the right almost negative value of the axial velocity in the core and yields a more confined vortex in better agreement with TUM experiments.

Figure 10 shows the axial velocity component at the cross-section x/c_r=0.475 for the NA1-W2 geometry. The IBV vortex has still a marked jet-type and DDES-SST is again the only model able to capture accurately the overshoot on the core axial velocity component, $k-\omega$ SST providing only a fair qualitative trend.

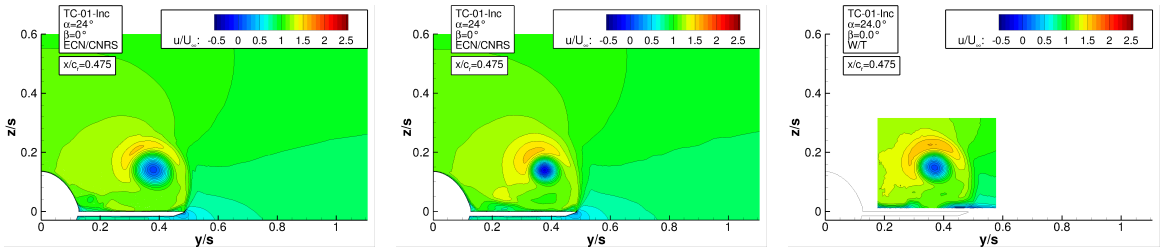

(a) k-ω SST. (b) DDES-SST. (c) TUM Experiments.

FIGURE 9 – $\beta = 0°$, $\alpha = 24°$, NA1-W1 - Axial component of the velocity at $x/c_r = 0.475$.

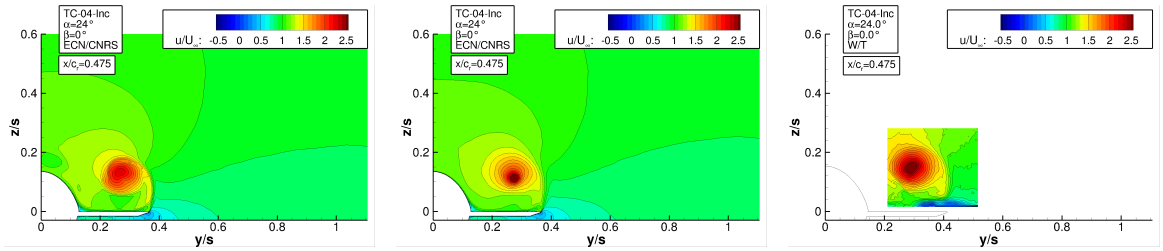

(a) k-ω SST. (b) DDES-SST. (c) TUM Experiments.

FIGURE 10 – $\beta = 0°$, $\alpha = 24°$, NA1-W2 - Axial component of the velocity at $x/c_r = 0.475$.

5.1.4 Angle of attack $\alpha = 32°$

Figure 11 presents the vortical structures obtained by the two turbulence models for the angle of attack $\alpha = 32°$ and both wing configurations. For both turbulence closures, the main IBV vortex exhibits a core fully contaminated with a reverse flow from its onset to its destabilisation for NA1-W1. Moreover, the MBV vortex seems to disappear quickly, at least as shown by the iso-Q* surface although we will see further from the cross-sectional views that it is still present. Two vortices emanate from the fuselage, instead of one for the previous angle of attack. These vortices are deviated towards the outer part of the wing at a location situated more upwind compared to the previous angle of attack but their interaction with the IBV is not visible in the cross-sectional views which will be shown next. For the NA1-W2 configuration, the global topology is very similar but the reverse flow in the core of IBV appears only at some distance from the onset, closer to the leading edge for DDES-SST than for k-ω SST.

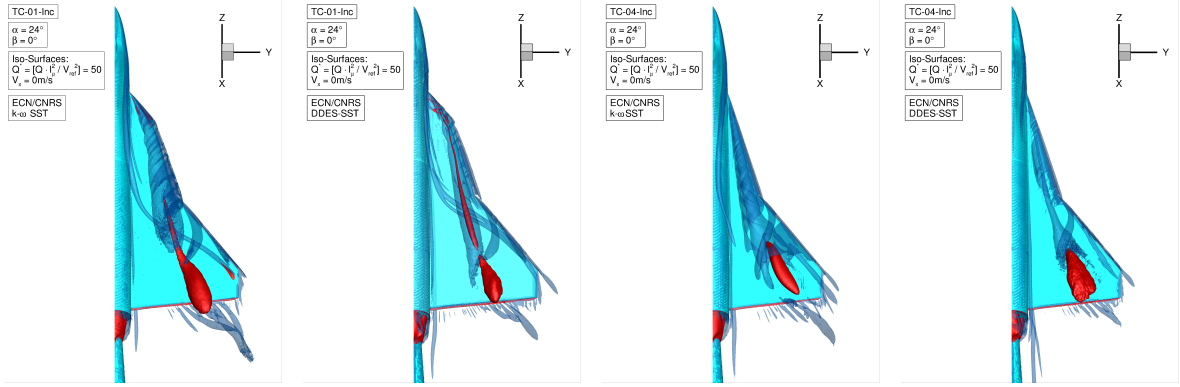

(a) NA1-W1 - k-ω SST. (b) NA1-W1 - DDES-SST. (c) NA1-W2 - k-ω SST. (d) NA1-W2 - DDES-SST.

FIGURE 11 – $\beta = 0°$ $\alpha = 32°$ - Vortical structures of the NA1-W1 and NA1-W2 configurations.

Figure 12 shows the axial velocity component at the cross-section x/c_r=0.475 for the NA1-W1 geometry. For this high angle of attack, TUM experiments reveal that the IBV vortex has a wake-type characteristic. The DDES-SST model is the model which provides the thinnest core. The area with a high velocity around the IBV vortex is underestimated with the k-ω SST model compared of the experimental data.

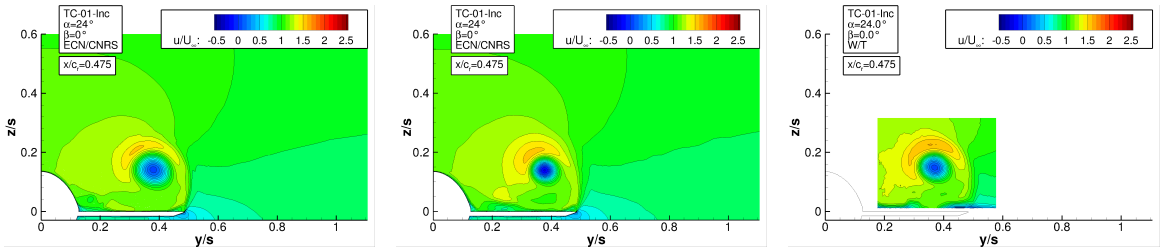

(a) k-ω SST. (b) DDES-SST. (c) TUM Experiments.

FIGURE 12 – $\beta = 0°$, $\alpha = 32°$, NA1-W1 - Axial component of the velocity at $x/c_r = 0.475$.

Figure 13 shows the axial velocity component at the cross-section x/c_r=0.475 for the NA1-W2 geometry. The k-ω SST model predicts a velocity level in the core of the vortex lower than in the experiments. The DDES-SST model predicts the correct level of the velocity in the core of the vortex. However, the position is not the same than in the experiments.

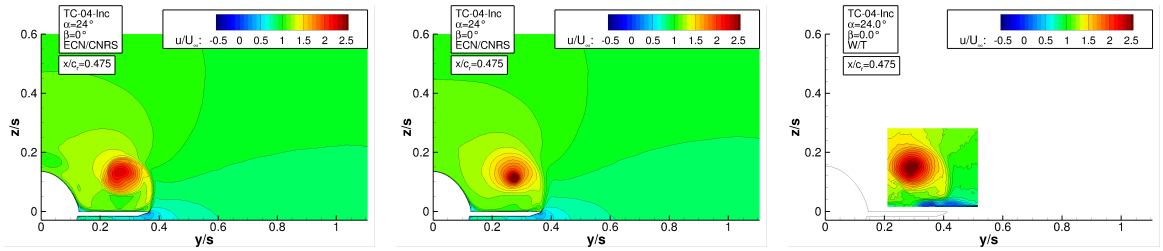

(a) k-ω SST. (b) DDES-SST. (c) TUM Experiments.

FIGURE 13 – $\beta = 0°$, $\alpha = 32°$, NA1-W2 - Axial component of the velocity at $x/c_r = 0.475$.

5.2 Sideslip angle condition : β = 5°

5.2.1 Forces and moments

Figure 14 presents the evolution of the longitudinal aerodynamic coefficients (the drag coefficient C_D, the lift coefficient C_L and the pitching moment coefficient C_{my}) versus the angle of attack, α, for both configurations. For the NA1-W1 geometry, see Fig. 14(a), the numerical results obtained with the k-ω SST and DDES-SST turbulence models are in good agreement with the experimental data. In the experiments, the vortex breakdown occurs at $\alpha = 15°$. For the NA1-W2 geometry, see Fig. 14(b), these aerodynamic coefficients are well predicted by both turbulence models and in good agreement with the experimental data, except at $\alpha = 32°$ where the k-ω SST model provides too high values compared to the experimental data.

The lateral aerodynamic coefficients (the side-force coefficient C_S, the pitching moment coefficient C_{mx} and the yawing moment coefficient C_{mz}) are presented in Fig. 15. For the NA1-W1 geometry, see Fig. 15(a), the agreement between the experimental data and the numerical results is less satisfactory than that obtained for the longitudinal aerodynamic coefficients. The side-force coefficient C_S and the

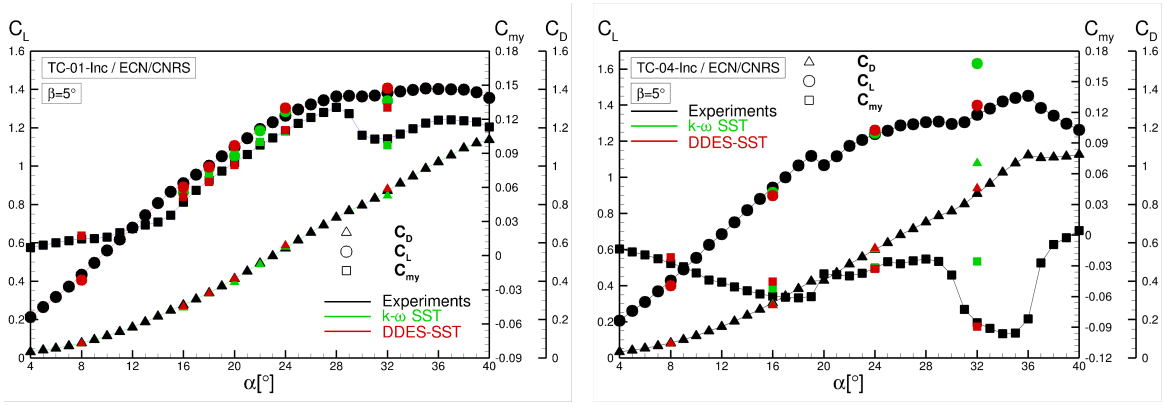

(a) NA1-W1 geometry. (b) NA1-W2 geometry.

FIGURE 14 – β = 5° - Longitudinal aerodynamics coefficients versus the angle of attack α for both geometries.

yawing moment coefficient C_{mz} are relatively well predicted by both turbulence models while the prediction of the rolling moment coefficient C_{mx} is inaccurate. The k-ω SST model is unable to predict the decay and the change of the slope observed experimentally around 16°. The DDES-SST model predicts the correct negative value at α = 16°. For α = 18°, C_{mx} increases as in experiments but for the higher angle of attack, the value decreases instead of keeping at constant value close to zero as in the experiments. For the very high value of angle of attack, α = 32°, the two turbulence models predict the positive value of C_{mx}, while C_S is hidden under $C_{mx}$for DDES-SST. For the NA1-W2 geometry, see Fig. 15(b), both turbulence models predict coefficients in agreement with the experimental data for the angles of attack α below 20°. For the higher angles, $\alpha \geq$ 24°, the k-ω SST model is unable to predict the monotonous decay of C_{mz} and for the C_S prediction, the value is in good agreement with the experimental data for α = 24° but it is strongly overestimated at 32°. As with the NA1-W1 wing profile, the behaviour of the rolling moment, with its change of sign around 20°, is not predicted with the k-ω SST model which predicts a decay. With the DDES-SST model, all lateral aerodynamic coefficients are well predicted and in good agreement with the experimental data, notably the change of sign of the rolling moment.

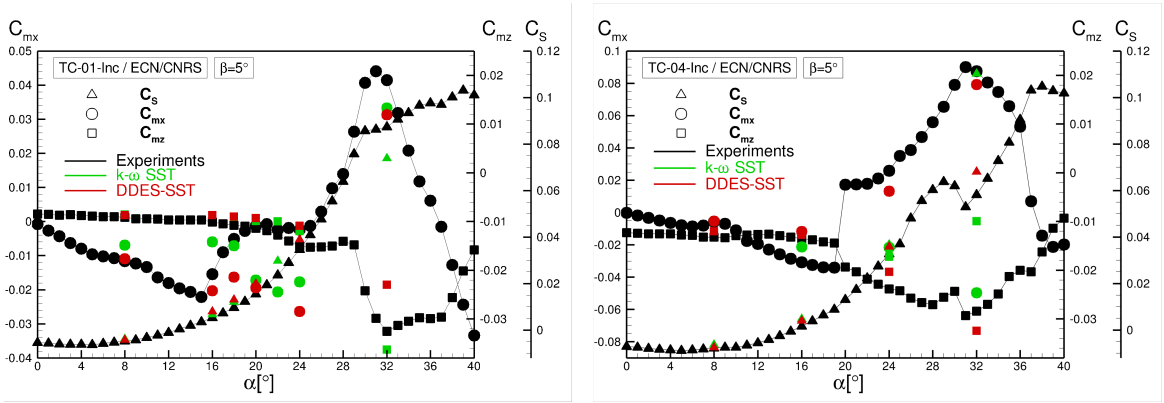

(a) NA1-W1 geometry. (b) NA1-W2 geometry.

FIGURE 15 – β = 5° - Lateral aerodynamics coefficients versus the angle of attack α for both geometries.

5.2.2 Angle of attack α = 16°

Fig. 16 shows the vortical structures for NA1-W1 and NA1-W2 geometries. The vortex developing in the front highly swept region is called the inboard vortex (IBV) and the vortex developing at the medium swept leading edge is called midboard vortex (MBV). With the DDES-SST model, the IBV vortices are thinner and more intense than those predicted with the k-ω SST model. With the NA1-W1 geometry, an area with a negative velocity, close to the onset of the wing, is predicted by both turbulence closures.

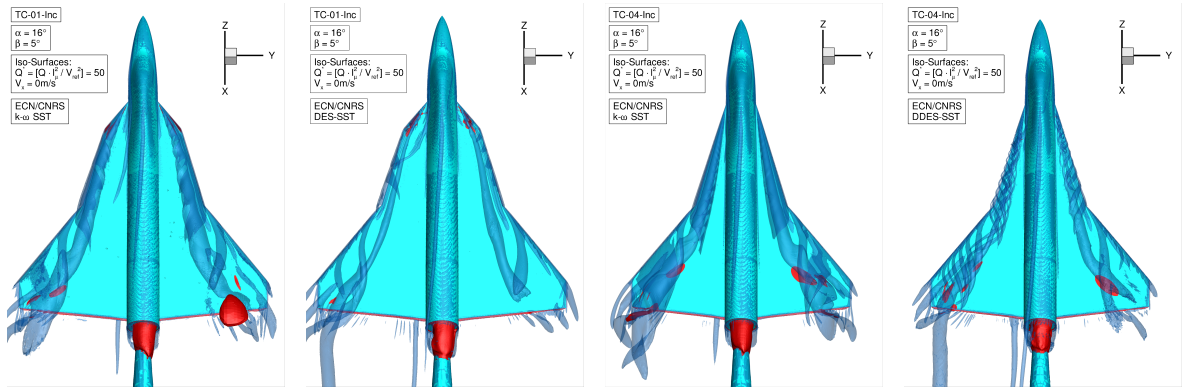

(a) NA1-W1 : k-ω SST. (b) NA1-W1 : DDES-SST. (c) NA1-W2 : k-ω SST. (d) NA1-W2 : DDES-SST.

FIGURE 16 – β = 5° , α = 16°- Vortical structures for the NA-W1 and NA1-W2 configurations.

The dimensionless axial velocity component at x/c_r = 0.475 is presented in Fig. 17 for the NA1-W1 geometry. In the experiments, on the leeward side, the IBV vortex has the characteristics of a jet-type vortex with a high axial velocity in the core of this vortex. On the windward side, the IBV has the characteristics of a wake-type vortex. For the numerical simulations, at windward side, the DDES-SST model predicts the low level of axial velocity and thus the wake-type vortex. It is not the case with the k-ω SST model. At leeward side, no turbulence model is able to predict the correct level of axial velocity in the IBV core. Both turbulence closures show two vortices very close to each other with opposite axial velocity. This feature is not observed in the experiments.

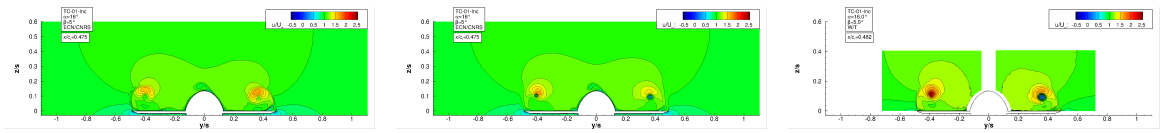

(a) k-ω SST. (b) DDES-SST. (c) TUM Experiments.

FIGURE 17 – β = 5° , α = 16° , NA1-W1 - Axial component of the velocity at x/c_r = 0.475.

Fig. 18 presents the dimensionless axial velocity distribution at x/c_r = 0.475 for the NA1-W2 geometry. For this geometry, the experiments show more symmetric vortices on each wings contrary to the NA1-W1 geometry. All vortices on the leeward side and the windward side have the jet-type characteristics. The k-ω SST model predicts a symmetric solution as in the experiments. However, the velocity in the IBV vortex core is lower than that obtained in the experiments. With the DDES-SST model, the level of axial velocity in the IBV vortex core at the leeward side is in agreement with the experimental data but at the windward side, the level is lower than the experiments. Thus the DDES-SST model predicts a asymmetric behaviour.

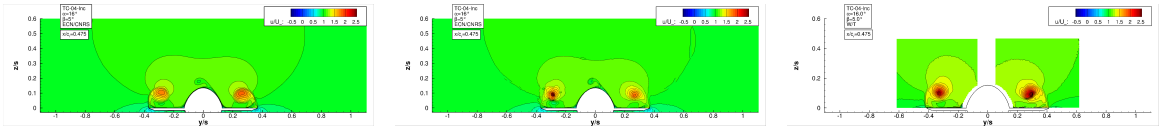

(a) k-ω SST. (b) DDES-SST. (c) TUM Experiments.

FIGURE 18 – β = 5° , α = 16° , NA1-W2 - Axial component of the velocity at x/c_r = 0.475.

5.2.3 Angle of attack α = 24°

Fig. 19 shows the vortical structures for both geometries, NA1-W1 and NA1-W2, at 24°. For the geometry NA1-W1, the DDES-SST model predicts more intense vortical structures on both leeward and windward wings. For this angle of attack, a flow reversal is observed in the inboard vortex, all along its trajectory on the windward wing while flow reversal occurs only close to the trailing edge of the leeward wing for both turbulence closures. For the geometry NA1-W2, the DDES-SST model predicts a more intense and stable IBV vortex on the leeward wing, leading to a more asymmetric vortical structures.

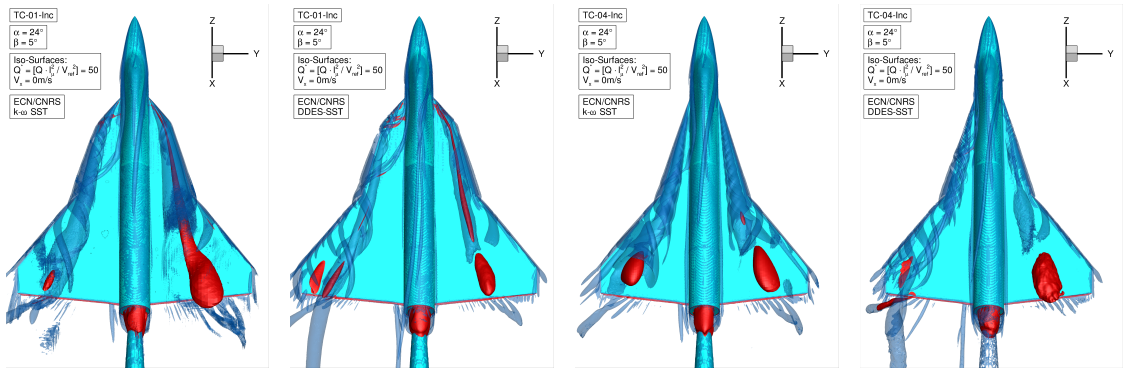

(a) NA1-W1 - k-ω SST. (b) NA1-W1 - DDES-SST. (c) NA1-W2 - k-ω SST. (d) NA1-W2 - DDES-SST.

FIGURE 19 – β = 5° , α = 24°- Vortical structures for the NA-W1 and NA1-W2 configurations.

Fig. 20 depicts the dimensionless axial velocity distribution at x/c_r = 0.475 for the NA1-W1 wing configuration. For the NA1-W1 configuration, the TUM experiments reveal an asymmetry of the vortices developing on each wing. On the leeward side, both IBV vortex is clearly jet-type vortex with a strong axial velocity in the core. The IBV vortex is similar between both numerical simulations but the jet-type vortex is not captured. Both turbulence closures predict the existence of two zones very close to each other corresponding to two co-rotating vortices, the upper one with a velocity overshoot and the lower one with a velocity undershoot. On the windward side, the IBV vortex observed experimentally is a wake-type vortex. Both turbulence closures are able to capture the strong decrease of the axial velocity in the core of the IBV vortex.

Fig. 21 presents the dimensionless axial velocity distribution at x/c_r = 0.475 for the NA1-W2 wing

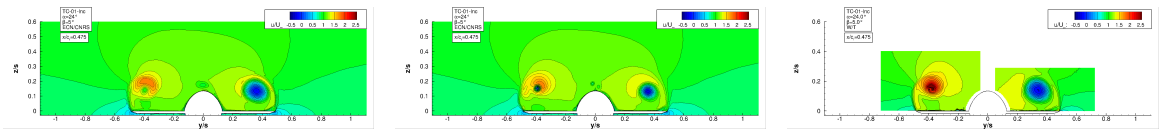

(a) k-ω SST. (b) DDES-SST. (c) TUM Experiments.

FIGURE 20 – β = 5° , α = 24° , NA1-W1 - Axial component of the velocity at x/c_r = 0.475.

configuration. As for the NA1 W1 geometry, the TUM experiments show an asymmetric situation characterised for the IBV vortex by a jet-type vortex on the leeward side and a wake-type vortex on the windward side while the MBV vortices keep their jet-type configuration. For the numerical simulations, at windward side, the level of the axial velocity in the IBV, obtained the k-ω SST model, is not in agreement with the experiments. Moreover, this model predicts an IBV vortex surrounded by a high axial velocity. With the DDES-SST model, the area of the low velocity in the IBV is lower than that obtained in the experiments. At the leeward side, the IBV vortex is under-estimated with the k-ω SST model. The DDES-SST model captures the right asymmetry of the flow even if the area of the high velocity is lower than that observed experimentally.

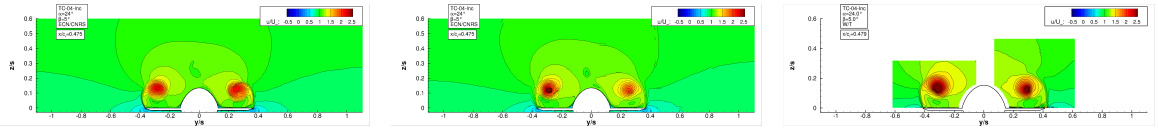

(a) k-ω SST. (b) DDES-SST. (c) TUM Experiments.

FIGURE 21 – β = 5° , α = 24° , NA1-W2 - Axial component of the velocity at x/c_r = 0.475.

5.2.4 Angle of attack α = 32°

Fig. 22 shows the vortical structures for both geometries and both turbulence closures. For the NA1-W1 geometry, a massive separation at the windward side is predicted by both turbulence models. However, this separation appears more intense with the DDES-SST model. At the leeward side, the result depends on the turbulence closure used. With the DDES-SST model, the flow reversal in the IBV vortex starts at mid-wing while with the k-ω SST, it starts close to the onset of the wing. For the NA1-W2 geometry, the two numerical simulations provide a different solution. At the windward side, the DDES-SST model predicts a massive separation as for the NA1-W1 geometry while the k-ω SST model predicts a longitudinal vortex with a zone of flow reversal. On the leeward wing, both numerical simulations predict longitudinal vortices as for the previous angle of attack and the vortices obtained with the DDES-SST model are thinner than those obtained with the k-ω SST model.

Fig. 23 depicts the dimensionless axial velocity distribution at x/c_r = 0.475 for the NA1-W1 geometry. The flow asymmetry becomes more important than that observed for 24° as shown by the experimental

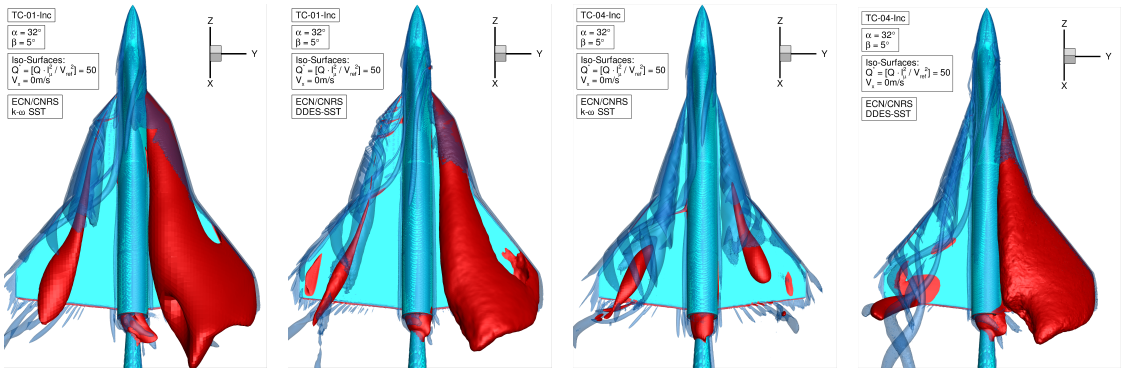

(a) NA1-W1 : k-ω SST. (b) NA1-W1 : DDES-SST. (c) NA1-W2 : k-ω SST. (d) NA1-W2 : DDES-SST.

FIGURE 22 – β = 5° ,α = 32°- Vortical structures for the NA-W1 and NA1-W2 configurations.

measurements. On the leeward side, a large zone with a low velocity is observed while at the leeward side the IBV vortex has a wake-type characteristics. Both numerical simulations reproduce this asymmetry of the flow. However, the k-ω SST model predicts a thicker IBV vortex at the leeward side. With the DDES-SST model, this vortex is thinner but this model is the only one able to predict the high velocity region above the IBV vortex, as observed in the experiments.

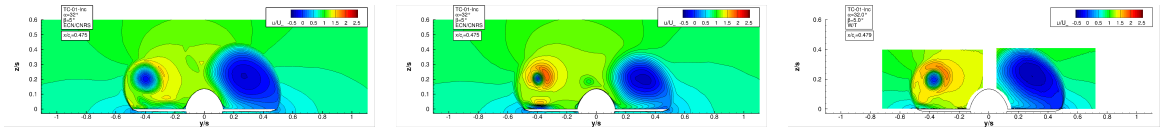

(a) k-ω SST. (b) DDES-SST. (c) TUM Experiments.

FIGURE 23 – β = 5° , α = 32° , NA1-W1 - Axial component of the velocity at x/c_r = 0.475.

Fig. 24 presents the dimensionless axial velocity distribution at x/c_r = 0.475 for the NA1-W2 wing configuration. In the experiments, at the windward side, a massive separation is predicted and at the leeward side,a jet-type vortex is observed. With the numerical simulations, the DDES-SST model is the only model able to predict the correct flow features for both wings of the aircraft. At the leeward side, the k-ω SST model predicts a thicker IBV vortex which is less intense than that observed in the experiments. At the windward side, the flow is characterised by a vortex with the k-ω SST model, contrary to the experimental observations.

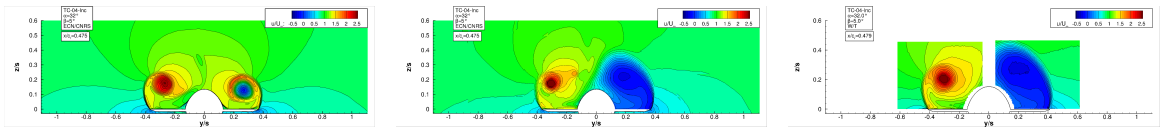

(a) k-ω SST. (b) DDES-SST. (c) TUM Experiments.

FIGURE 24 – β = 5° , α = 32° , NA1-W2 - Axial component of the velocity at x/c_r = 0.475.

6 Conclusions

In this paper, a study of the flow around two different wing configurations, the so-called NA1-W1 and NA1-W2 geometries, for several angles of attack and two drift angles, has been presented. Two turbulence closures were used : the k-ω SST and the hybrid RANS/LES DDES-SST models. Numerical simulations were run using flow-adapted grids to capture automatically the vortical structures during their evolution. This functionality is a very precious specificity of the flow solver ISIS-CFD for this category of computations. Comparisons of aerodynamic coefficients, local flow details and vortex core analysis were conducted with the TUM experiments.

For the symmetric condition, the simulation performed with the DDES-SST model is globally equivalent to the one performed with the k-ω SST model for low angles of attack. For high angles of attack, the hybrid RANS/LES model clearly shows its superior reliability. The NA1-W2 geometry appears easier to simulate than the NA1-W1 geometry.

The sideslip condition appears more complex to simulate for both configurations, although a better agreement with TUM experiments is observed for the NA-W2 geometry. The change of sign of the rolling moment is indeed a challenge for turbulence models. For the NA1-W2 geometry, the DDES-SST model is the only one able to predict this change of sign around the angle of attack α = 20°. This change of

sign of the rolling moment is due to an asymmetric behaviour of longitudinal vortices on the leeward and windward sides. For the NA1-W1 geometry, the rolling moment change of sign is not satisfactorily predicted by both turbulence closures. This incorrect prediction is probably due to the early interaction between the fuselage vortex and the IBV vortex, not far from the onset of the wing.
Finally, while the use of hybrid RANS/LES models is the only viable option to accurately predict the change of rolling stability, the computations should obligatorily be performed with anisotropic adaptive mesh refinement, since this is the only possibility to maintain the fine grid density in the core of the various interacting vortices and keep the computational effort for industrial studies within high but reasonable limits.

Acknowledgment

The computations were performed using HPC resources from GENCI (Grand Equipement National de Calcul Intensif) which is gratefully acknowledged.

References

[1] C. Breitsamter. Unsteady flow phenomena associated with leading-edge vortices. *Progress in Aerospace Sciences*, 44 :48–65, 2008.

[2] R.-D. Cecora, R. Radespiel, B. Eisfeld, and A. Probst. Differential Reynolds-Stress Modeling for Aeronautics. *AIAA Journal*, 53(3) :739–755, 2015.

[3] G. B. Deng and M. Visonneau. Comparison of explicit algebraic stress models and second-order turbulence closures for steady flow around ships. In *7th Symposium on Numerical Ship Hydrodynamics*, pages 4.4–1–15, Nantes, France, July 1999.

[4] R. Duvigneau, M. Visonneau, and G. B. Deng. On the role played by turbulence closures in hull ship optimization at model and full scale. *Journal of Marine Science and Technology*, 8 :11–25, 2003.

[5] E. Guilmineau, G. B. Deng, A. Leroyer, P. Queutey, M. Visonneau, and J. Wackers. Assessment of hybrid RANS-LES formulations for flow simulation around the Ahmed body. *Comupters & Fluids*, 178 :302–319, 2018.

[6] S. M. Hitzel. Combat Aircraft Vortex Interaction - Design, Pysics & CFD-Tools. In *SciTech AIAA*, San Diego, CA, 2022. American Institute of Aeronautics and Astronautic. AIAA 2022-0156.

[7] S. M. Hitzel, A. Winkler, and A. Hövelmann. Vortex Flow Aerodynamic Challenges in the Design Space for Future Fighter Aircraft. In A. Dillman, G. Heller, E. Krämer, C. Wagner, C. Tropea, and S. Jakirlic, editors, *New results in Numerical and Experimental Fluid Mechanics XII. DGLR 2018. Notes on Numerical Fluid Mechanics and Multidisciplinary Design*, volume 142, pages 297–306. Springer, Cham, 2020.

[8] A. Leroyer and M. Visonneau. Numerical methods for RANSE simulations of a self-propelled fish-like body. *Journal of Fluids and Structures*, 20 :975–991, 2005.

[9] J. M. Luckring, M. A. Park, S. M. Hitzel, A. Jirásek, A. J. Lofthouse, S. A. Morton, D. R. McDaniel adn A. Rizzi, and M. Tomac. a Synthesis of Hybrid RANS/LES CFD Results for F-16XL Aircraft Aerodynamics. *Journal of Aircraft*, 54 :2100–2114, 2017.

[10] S. Mozaffari, E. Guilmineau, M. Visonneau, and J. Wackers. Average-based mesh adaptation for hybrid RANS/LES simulation of complexe flows. *Computers and Fluids*, 232 :105202, 2022.

[11] S. Pfnür and C. Breitsamter. Leading-Edge Vortex Interactions at a Generic Multiple Swept-Wing Aircraft. *Journal of Aircraft*, 56(6) :2093–2107, 2019.

[12] P. Queutey and M. Visonneau. An interface capturing method for free-surface hydrodynamic flows. *Computers and Fluids*, 36 :1481–1510, 2007.

[13] M. Visonneau, E. Guilmineau, and G. Rubino. Local flow around a surface combatant at various static drift conditions : The role played by turbulence closures. In *33rd Symposium on Naval Hydrodynamics*, Osaka, Japan, 2020.

[14] J. Wackers, G. B. Deng, E. Guilmineau, A. Leroyer, P. Queutey, and M. Visonneau. Combined refinement criteria for anisotropic grid refinement in free-surface flow simulation. *Computers and Fluids*, 92 :209–222, 2014.